Templateless Synthesis of Ultramicroporous 3D Graphitic Carbon from Cyclodextrins and their use as Selective Catalyst for Oxygen Activation

Alejandra Rendón-Patiño,[a] Andrea Santiago-Portillo,[a] Cristina Vallés-Garcia,[a] Miguel Palomino,[a] Sergio Navalón,[a] Antonio Franconetti,[b] Ana Primo*[a] and Hermenegildo Garcia*[a]

PhD A. Rendón-Patiño, Dr. A. Santiago-Portillo, PhD C. Vallés-García, Dr. M. Palomino, Dr. S. Navalón, Dr. A. Franconetti, Dr. A. Primo, Prof. Hermenegildo García.

[a] Instituto de Tecnología Química (CSIC-UPV) and Department of Chemistry, Consejo Superior de Investigaciones Científicas-Universitat Politècnica de Valencia, Avenida de los Naranjos s/n, 46022 Valencia, Spain

[b] Departamento Química Orgánica, Facultad de Química, Universidad de Sevilla, Profesor García Gonzalez 1, 41012 Sevilla, Spain

Emaills: aprimoar@itq.upv.es; hgarcia@qim.upv.es

Abstract.

Pyrolysis of $\alpha-$, $\beta-$ and $\gamma-$cyclodextrins at 900 ^{o}C gives rise to the formation of crystalline graphitic porous nanoparticles (G_{CD}), where the dimensions of the pores are uniform in the range from 0.63 to 0.97 nm from $G_{\alpha-CD}$ to γ $G_{\gamma-CD}$ as determined by transmission electron microscopy. It was found that, while for $G_{\gamma-CD}$ and $G_{\gamma-CD}$ the surface area measured by N_2 adsorption was about 330 to 550 $m^2 \times g^{-1}$, respectively, no area can be measured for $G_{\alpha-CD}$ with N_2 or Ar due to its small pore dimensions. However, CO_2 adsorption reveals for $G_{\alpha-CD}$ the presence of ultramicroporosity and a surface area of 727 $m^2 \times g^{-1}$. G_{CD} exhibit activity as metal-free catalysts for the aerobic oxidation of alcohols and the activity increases as the pore dimensions decreases. DFT calculations on models indicates that this

high catalytic activity for O_2 activation derives from confinement effects that favors charge transfer from the graphitic walls to O_2. Studies on the formation mechanism shows that the key step leading to the formation of the channels is the melting of cyclodextrins precursors that makes possible the assembly of these capsules before their transformation into microporous graphitic particles.

Introduction.

Due to their large specific surface area in a small footprint, there is an increasing interest in structuring graphitic carbon as a tridimensional porous material with possible applications as electrocatalysts, supercapacitors and batteries.[1-3] These 3D porous graphitic materials can be obtained by following two general methodologies, either the use of hard templates or hydrothermal treatment.[1-3]In the majority of the cases, preformed graphene or graphene oxide were used as precursors in the formation of the 3D graphene, but chemical vapor deposition (CVD) synthesis using volatile precursors has also been reported.[1, 4] The target in this field is to obtain 3D graphitic powdered materials with large surface area approaching the theoretical value for a solid with walls constituted by single layer graphene, high mechanical stability and uniform pore size in the subnanometric range. [3]

Pyrolysis of sucrose, saccharides and polysaccharides may render graphitic carbon residues.[5, 6] In a series of papers, it has been shown that powders of natural polysaccharides can form, after pyrolysis at temperatures above 800 ^{o}C, graphitic particles that upon exfoliation render in a high yield defective graphenes. [7-9] Defects in these graphenes consist in oxygenated functional groups, due to the residual O content of the graphene.[7, 10, 11] Other possible defects are carbon vacancies generated during the pyrolysis by evolution of CO_2, CO and other gases. [7, 10, 11] It has been typically found that the morphology of the precursor particles is maintained during the pyrolysis step, although particle dimensions shrink, even more than a half, due to the restructuring of the intermolecular distances and occurrence of $\pi-\pi$ stacking.[12] Continuing with this line of research, it would be of interest to determine

if other saccharides with peculiar morphology can also become transformed into some sort of graphitic carbon and which is the structure and properties of the resulting material.

In this context, cyclodextrins are cyclic oligomers of glucose with a number higher than five units, the most convenient ones being α, β and γ cyclodextrin, with six, seven and eight glucose monomers, respectively.[13, 14] The difference in the number of glucose units determines the diameter of the organic capsule in the subnanometric scale. These organic molecules are soluble in water, but the less polar interior is appropriate to form in aqueous media supramolecular host (cyclodextrin)-guest complexes with aromatic hydrocarbons and other types of molecules, provided that their size is smaller than the pore aperture.[15, 16] Considering that cyclodextrins are widely available carbohydrates with a defined hollowed capsule morphology and that some acyclic carbohydrates can act as precursors of graphenes, [5, 6] it is of interest to submit cyclodextrins to pyrolysis to further advance in the knowledge of the structure and porosity of the resulting carbon residues and to determine their catalytic activity as a function of the precursor size. It was anticipated that, if formed, the pore dimensions of these materials would be correlated somehow with the dimensions of the α, β and γ cyclodextrin used as precursor and this pore dimension can influence their catalytic activity. In one related precedent, formation of rod-like graphitic carbon nanostructures (microns length tubes, 10-40 nm diameter) evolving from *structureless carbon* was reported by pyrolysis of α−cyclodextrin at temperatures higher than 1000 ºC.[17] However, no attention was paid to the structure of the carbon nanorod precursor that appears at lower temperatures. In another study, α, β and γ cyclodextrins and 6-deoxy β−cyclodextrin derivatives were submitted to pyrolysis as models of cellulose degradation,[18] but the focus was on the analysis of the volatile products and not on the structure of the resulting carbons. [18]

Besides these two isolated precedents, the structure and catalytic activity of the carbon residues from cyclodextrins obtained at temperatures below 1000 ºC remain undisclosed and their possible catalytic activity ignored. Particularly important is to determine the porosity and nature of the carbon material. As it would be shown later, TEM imaging and spectroscopic evidences, show that

pyrolysis of α, β and γ cyclodextrins at 900 °C renders microporous 3D graphitic materials whose porosity depends on the precursor dimensions. These 3D graphitic materials exhibit catalytic activity to promote aerobic oxidations with an activity that correlates with the size of the micropores. Theoretical calculations provide a rationalization of the influence of pore size on gas adsorption and the reasons why activation of molecular oxygen occur easier when the dimensions of the pores are commensurate with the size of molecular oxygen.

Results and discussion.

Pyrolysis of α, β and γ cyclodextrins as powders was carried out in an electrical oven, heating at 5 °C·min^{-1} up to 900 °C with a holding time of 2 h. In agreement with the thermogravimetric profiles (Figure 1a, inset), a weight loss about 80 % was measured for the three cyclodextrins under study. This weight loss indicates that besides oxygen and hydrogen, about 50 % of the carbon atoms are also removed in the pyrolysis, probably mostly as CO_2, since otherwise the remaining mass of the carbon residue should have been 44 %. Similar thermogravimetric profiles as the one measured here have been previously determined. [17-19]

Combustion chemical analysis of the graphitic carbon residues (G_{CD}) obtained by pyrolysis of α, β and γ cyclodextrins indicates that they are constituted predominantly by carbon (see Table 1), but that there is still a significant percentage of residual oxygen, particularly for $G_{\beta-CD}$ and $G_{\gamma-CD}$. In the case of $G_{\alpha-CD}$ the carbon content was the highest ever reported for graphitic carbons derived from pyrolysis of carbohydrates.[11] Worth noting is the fact that the presence of small percentages of adventitious nitrogen was observed for the three samples. Since the molecular formula of cyclodextrins does not contain N, the source of this minute N percentage detected for the three G_{CD} by combustion analysis was intriguing. To determine the origin of N, the commercial samples of the three cyclodextrins were also submitted to combustion analysis, observing the presence of a minute N percentage, of 0.01, 0.01 and 0.02 % for α-, β- and γ-CD, respectively barely in the detection limit of

the equipment. It is proposed that this minute N impurity is due to the imperfect purification of cyclodextrins after their enzymatic preparation, N becoming concentrated by a factor of 10 during the pyrolysis. Since N atoms on graphene are known to act as catalytic sites for certain reactions,[20] their possible role in promoting the aerobic oxidation should be considered. It should be noted, however, that the N content of the three samples is very similar within 0.07 % difference.

Raman spectra of the three G_{CD} samples were similar, exhibiting three peaks appearing at 2800 (broad), 1590 and 1350 cm^{-1} corresponding to the expected 2D, G and D peaks, respectively, characteristic of defective graphenes.[21, 22] Figure XX in the supporting information presents the Raman spectra for the three G_{CD} under study. The relative intensity of the G vs the D band (I_G/I_D) in the three G_{CD} ranges from 1.15 to 1 that is in accordance with the I_G/I_D ratios reported for other defective graphenes obtained by pyrolisis of carbohydrates.[7, 8, 10, 23] As an example, Figure S1 shows an illustrative Raman spectra for $G_{\alpha-CD}$.

Surface area and porosity measurements were carried out initially by isothermal N_2 absorption at 77 K. The results are also given in Table 1. As it can be seen there, specific surface area values of 331 and 454 m$^2 \cdot$g^{-1} were measured for $G_{\beta-CD}$ and $G_{\gamma-CD}$, with a pore size about 2.3 nm. Figure S2 shows a representative N_2 absorption plot and the corresponding pore size distribution determined from the desorption branch. Importantly, similar type of measurements for $G_{\alpha-CD}$ did not give any area value. We speculated that this could be due to the small pore size of $G_{\alpha-CD}$ that would be impossible to be determined by N_2 absorption. To provide evidence in support of this claim, porosity of $G_{\alpha-CD}$ was also measured using Ar at 77 K and also a specific surface area value of 0 m$^2 \cdot$g^{-1} was obtained. On the contrary, the surface area of $G_{\alpha-CD}$ was measured by CO_2 absorption and a value of 727 m$^2 \cdot$g^{-1} and narrow pore distribution of 7.5 Å is obtained (See Figure S3 in supporting information). Analogous measurements were also carried out for $G_{\beta-CD}$ and $G_{\gamma-CD}$. The corresponding values are also included in Table 1. As it can be seen there, for the three G_{CD} samples under study, the specific surface area determined by CO_2 adsorption at 273 K was higher than that estimated by N_2 adsorption at 77 K. The

most remarkable case was, however, that of $G_{\alpha\text{-CD}}$. There are precedents in the literature showing differences in specific surface area values depending on the use of N_2, Ar or CO_2 that are attributed to the different kinetic diameter of CO_2 (0.300 nm), Ar (0.340 nm) and N_2 (0.364 nm) and the different adsorption temperatures,[24, 25] the first being able to measure ultramicroporosity,[25] i.e., pores below 0.5 nm diameter. It is proposed that the same is happening in the present case, the discrepancy between the absence of porosity in the N_2 and Ar measurement with the CO_2 adsorption being due to the exquisite discrimination of the pores of $G_{\alpha\text{-CD}}$ between both gases. In this way, the difference between the specific surface area values measured by CO_2 and N_2 is attributed to the surface area corresponding to ultramicropores.[26, 27] We will come back later to this issue when describing the theoretical models for G_{CD} and the reasons for their higher activity of $G_{\alpha\text{-CD}}$ to promote catalytic O_2 oxidations in comparison to the other congeners.

Table 1. Analytical and textural data of graphitic carbon residues obtained by pyrolysis of α, β and γ cyclodextrins

Sample	% C[a]	% N[a]	Surface area (m²/g)[b]	Pore volume (cm³/g)[b]
$G_{\alpha\text{–CD}}$	95.44	0.20	0 (727.54)	0
$G_{\beta\text{-CD}}$	88.06	0.13	331.01 (596.76)	0.163
$G_{\gamma\text{-CD}}$	87.41	0.14	453.65 (632.05)	0.223

[a] It is assumed that the rest to 100 % is residual oxygen; [b] Measured from N_2 adsorption, the number in brackets is obtained from CO_2 adsorption measurements.

XRD of the resulting carbon material after the pyrolysis indicates that it corresponds to a poorly crystalized graphitic carbon, observing broad peaks at 2Θ 25 and 42 º. Even more importantly, a sharp

peaks at 11.92 $^{\circ}$ for $G_{\alpha\text{-CD}}$, at 4.45 $^{\circ}$ for $G_{\beta\text{–CD}}$ and 4.25 $^{\circ}$ for $G_{\gamma\text{–CD}}$ were recorded (Figure 1, b, c and d). Figure XX in the supporting information provides an expansion of the short angle region for the diffraction patterns of $G_{\beta\text{-CD}}$ and $G_{\beta\text{-CD}}$, where the minor shift in the position of the peaks can be seen. It is proposed that these peaks correspond to the assembly of the cyclodextrin units generating a regular channel structure. The diameter of the channel can be determined applying the Bragg equation to this peak corresponding to a pore diameter of 0.74 for $G_{\alpha\text{-CD}}$, while they increase in dimension for $G_{\beta\text{-CD}}$ and $G_{\gamma\text{-CD}}$ Observations of this low-angle diffraction peak is unique and it has not been previously observed for any of the graphitic carbon residues derived from polysaccharides.[17] Another notable difference between G_{CD} and the graphitic carbon residues derived from pyrolysis of polysaccharides was that in the case of natural polysaccharides constituted by polymeric fibrils, the graphitic residue can be efficiently exfoliated upon sonication, forming suspensions of defective graphenes in quite high yield.[7] However, in the present case, sonication of the carbon residues from cyclodextrins (G_{CD}) does not result in exfoliation and it was not possible to obtain significant yields of persistent single or few layers graphene suspensions upon prolonged high-power ultrasound treatment of G_{CD}. This point will be commented later when discussing the structure of G_{CD} determined by electron microscopy images.
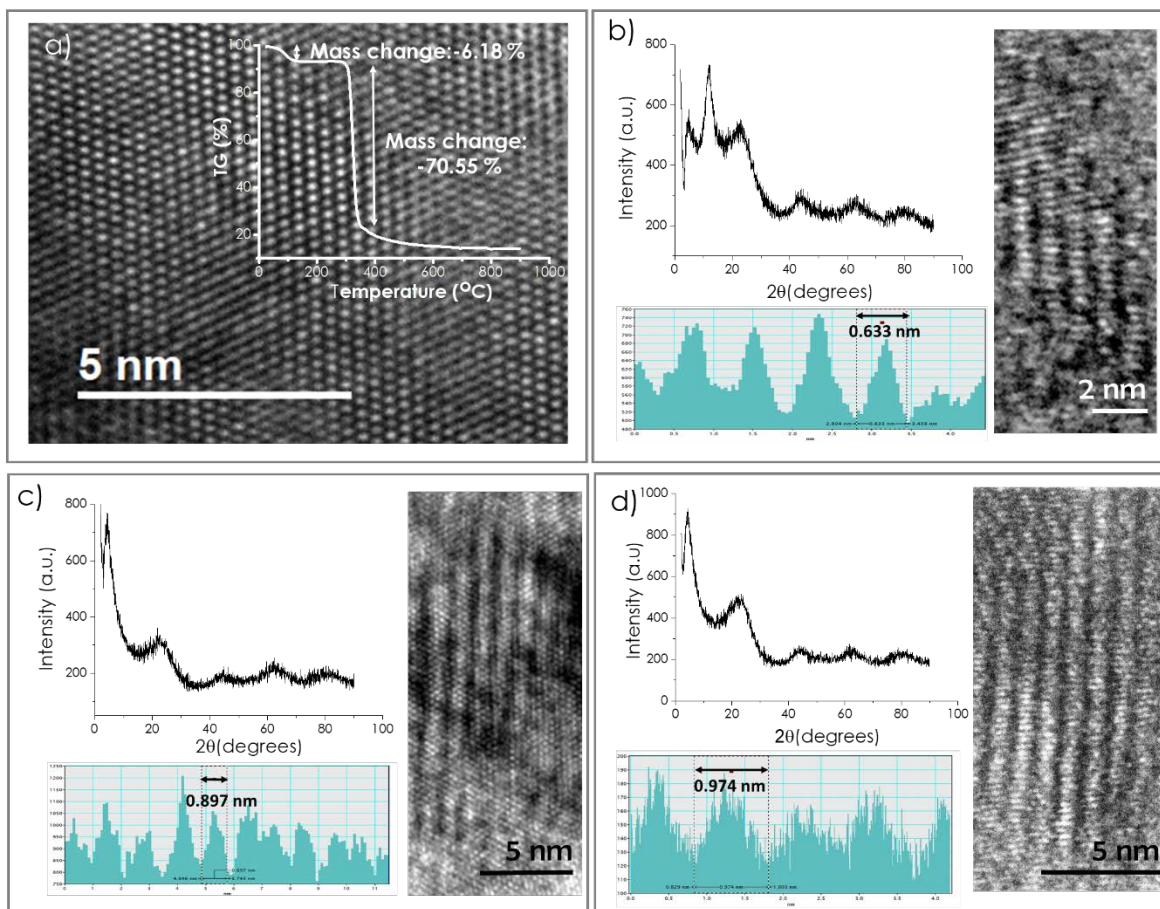
Figure 1. a) High resolution TEM image showing the high crystallinity of $G_{\alpha\text{-CD}}$. Inset: Thermogravimetric profile under N_2 of $G_{\alpha\text{-CD}}$. XRD, TEM images showing the channel structure and the dimensions of the corresponding channels of b) $G_{\alpha\text{-CD}}$ c) $G_{\beta\text{–CD}}$ and d) $G_{\gamma\text{–CD}}$.

The structure of G_{CD} and the differences among them as a function of the cyclodextrin precursor are clearly revealed by transmission electron microscopy (TEM). Figure 1 shows selected images to illustrate the high crystallinity of the material, indicating that they correspond to graphitic carbons. Importantly, the presence of channels was clearly observed in the three samples. By measuring the periodic contrast fluctuation in the image between wall and pore, the dimensions of these channels were estimated as 0.633, 0.807 and 0.974 nm for $G_{\alpha\text{-CD}}$, $G_{\beta\text{–CD}}$ and $G_{\gamma\text{–CD}}$, respectively (see Figure 1). Based on these TEM measurements, a constant increment of about 0.17 nm was

calculated for each additional glucose unit in the cyclodextrin precursor from α to γ. According to these TEM images and the microporosity observed in gas adsorption, it is proposed that these channels are derived from the assembly of conical cyclodextrin capsules as tubes during the pyrolysis process as depicted in Scheme 1. It has been previously observed that the conical shape of cyclodextrins favors their assembly as tubes under certain conditions in solution[17] and it could be that the same type of arrangement occurs in the cyclodextrin crystals that should melt during the process for a certain period (estimated melting point of cyclodextrins between 260 and 300 ^{o}C)[18] before occurrence of the profound chemical transformation leading to G_{CD}. According to Scheme 1, the cyclodextrin melt and the high temperatures should allow molecular arrangement as microtubules that undergo fusion into channels in subsequent steps.
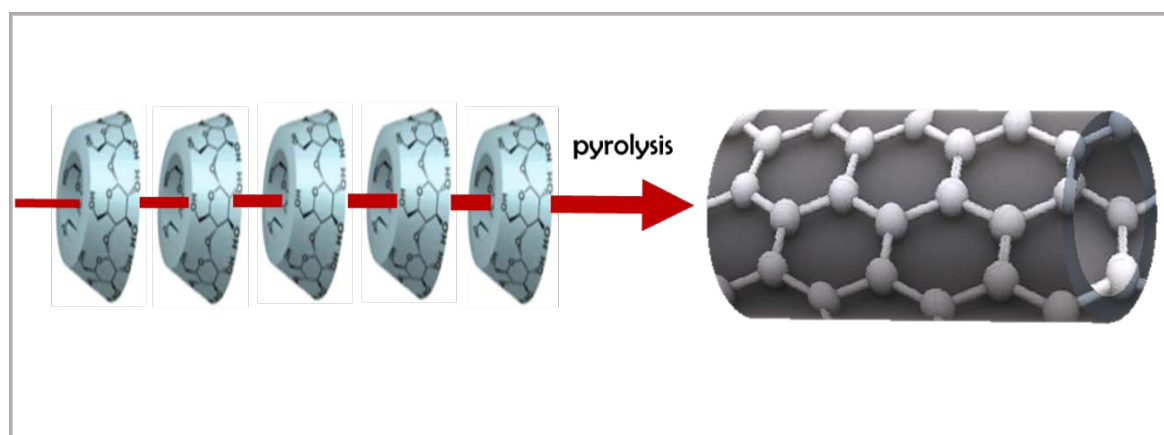
Scheme 1. Pictorial illustration of the assembly of conical cyclodextrin capsules as graphitic tubes during the pyrolysis process.

To provide some support to this hypothesis, α, β and γ cyclodextrins were melt at 300 ^{o}C and this temperature held during 2 h. After this time, the samples were cooled down at ambient temperature and the resulting annealed solids were analyzed by XRD and TEM. Figure S4 in the supporting information provides the XRD patterns of commercial cyclodextrins and those recorded after melting and 2 h annealing compared to those of G_{CD}. As it can be seen in Figure S4, the XRD

patterns of the cyclodextrins after melting are similar to those of the graphitic carbon residues G_{CD} and totally different from those of the commercial powders. This similarity after the melt and those of G_{CD} indicates that structuration into channels can occur in the melt. This proposal was further confirmed by TEM images of the cyclodextrins that were melt at 300 $^{\circ}$C and, then, cooled down at room temperature. Figure XX in the supporting information shows a representative set of these images, where the presence of the channels due to assembly of the cyclodextrins in the liquid phase can be clearly seen.

Catalytic activity

One of the main applications of defective graphene and related graphitic carbons is as metal-free catalyst.[28, 29] Among the different types of reactions that can be promoted by defective graphenes, aerobic oxidation of hydrocarbons and alcohols is among of the most general ones.[29] Therefore, it was of interest to determine the catalytic activity of G_{CD} for this type of reaction and particularly if there is an influence of the pore size in the critical range distinguishing gas molecules on the catalytic activity. In the most general reaction mechanism, molecular oxygen is activated by the catalyst forming superoxide or other reactive oxygen species that are able to trigger a reaction chain mechanism.

Aimed at determining the catalytic activity of G_{CD} for aerobic oxidations, benzylic alcohol was selected as probe molecule. The reactions were carried out in toluene at 160 $^{\circ}$C under 5 bar O_2 pressure, in the absence of any base. Figure 2a shows the time-conversion plot for the aerobic oxidation of benzyl alcohol. Benzyl alcohol was converted into a mixture of benzaldehyde, benzoic acid and benzyl benzoate, with selectivity values depending on the conversion (see Figure S5 in supporting information). A clear relationship between the nature of the precursor and the catalytic activity of the resulting G_{CD} was observed. Thus, the relative activity order was $G_{\alpha-CD} > G_{\beta-CD} > G_{\gamma-CD}$. A

comparison with the activity of commercial active carbon shows that any of the G_{CD} is a more efficient catalyst than active carbon.
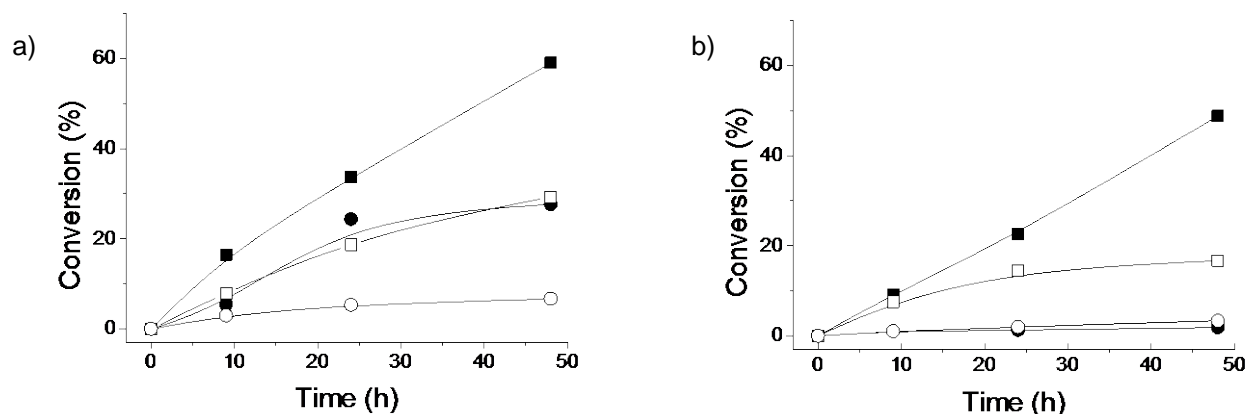

Figure 2. Time conversion plots for aerobic oxidation of a) benzyl alcohol and b) 1-phenylethanol using the catalysts: ■ $G_{\alpha\text{-}CD}$, □ $G_{\beta\text{-}CD}$, ● $G_{\gamma\text{-}CD}$ or ○ carbon activated. Reaction conditions: benzyl alcohol or 1-phenylethanol 1mmol, toluene2.5 mL, catalyst 10 mg, O_2 pressure 5 bars, temperature 160 ºC.

Recyclability tests by using the same $G_{\alpha\text{-}CD}$ sample in consecutive reactions indicate a gradual deactivation of the catalyst upon reuse (see Figure S6 in supporting information). Since reuse tests without toluene washings of the used $G_{\alpha\text{-}CD}$ catalyst results in a complete deactivation and the activity of the used $G_{\alpha\text{-}CD}$ catalyst depends largely on the washing process, it is proposed that the main deactivation pathway is clogging of the $G_{\alpha\text{-}CD}$ pores by substrate and products. Particularly carboxylic acids are well known poisons by strong interaction with the catalyst active sites.

Working under the same reaction conditions, the same activity order was measured for the aerobic oxidation of 1-phenylethanol that was selectively converting into acetophenone (Figure 2b). As in the case of benzyl alcohol, also for 1-phenylethanol, the commercial active carbon was notoriously inefficient to promote this aerobic oxidation. Although an almost complete conversion of 1-phenylethanol to acetophenone was observed at long reaction times using $G_{\alpha\text{-}CD}$ as catalyst, the reaction was significantly slower as compared to benzyl alcohol oxidation (compare plots in Figure 2).

This slower reactivity of 1-phenylethanol is proposed to be due to the steric encumbrance of secondary alcohols compared to primary alcohols. The aerobic oxidation of benzylic alcohol was also expanded to *para* substituted derivatives (Figure 3a). It was observed that 4-methoxybenzyl alcohol undergoes selective oxidation to the corresponding *p*-methoxybenzaldehyde somewhat faster than the parent benzyl alcohol, while 4-methylbenzyl alcohol undergoes oxidation significantly slower affording a mixture of 4-methylbenzaldehyde, 4-methylbenzoic acid and 4-methylbenzyl 4-methylbenzoate with selectivity values depending on the conversion (see Figure S5 in supporting information).
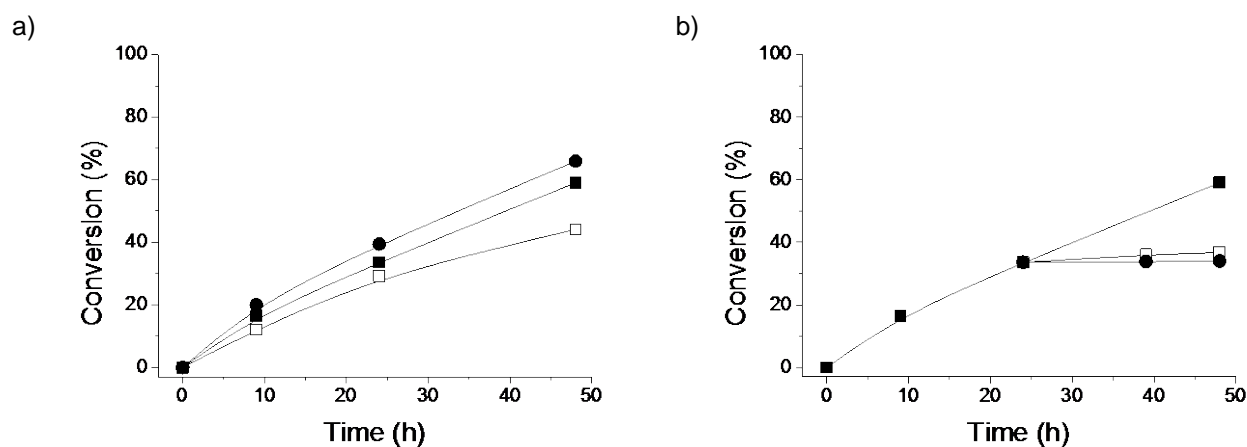

Figure 3. a) Time conversion plot for aerobic oxidation of different para substituted derivatives of benzyl alcohol ■) H □) CH$_3$ ●) CH$_3$O using G$_{\alpha\text{-CD}}$ as catalyst; b) Time conversion plot for aerobic oxidation of benzyl alcohol using G$_{\alpha\text{-CD}}$ as catalyst in the presence of different selective quenchers of reactive oxygen species ■) without quencher; □) 20 % DMSO; ●) 20 % p-benzoquinone.

The performance of G$_{\alpha\text{-CD}}$ as heterogeneous catalysts for aerobic oxidation of alcohols was also tested under the same conditions for aliphatic primary (1-octanol) and secondary (2-octanol) alcohol oxidation to the corresponding carbonylic compounds. In accordance with the expected relationship between the alcohol structure and reactivity, aliphatic alcohols undergo conversion to the corresponding carbonyl compounds at slower rate (see Figure S7 in supporting information), although a significant conversion was still achieved even for these aliphatic substrates at low reaction times.

Regarding the reaction mechanism and particularly the nature of the reactive oxygen species involved on the aerobic alcohol oxidation, a series of benzyl alcohol oxidation reactions were carried out under the typical reaction conditions. In these reactions selective quenchers were added at 10 h reaction, when the conversion was about 40 %, to see their influence on the reaction evolution. The fact that the reaction was already initiated in the absence of quenchers ensures that all the possible oxygen reactive species involved have already been generated in the reaction mixture and have reached a steady-state concentration. The amount of quencher added to the reaction was 20 mol% respect to the initial amount of benzyl alcohol. Since reactions involving reactive oxygen species are typically radical chain mechanisms, the presence of quencher in this proportion should be reflected in a significant change in the temporal conversion profile after its addition. As selective quenchers, *p*-benzoquinone to inhibit superoxide ($O_2^{\cdot-}$)[30-33] and dimethylsulfoxide (DMSO)[34-36] to intercept hydroxyl radicals ($\cdot$OH) were used. The results are presented in Figure 3b. As it can be seen there, the reaction completely stops using *p*-benzoquinone as quencher indicating that $O_2^{\cdot-}$ formed by single electron reduction of molecular dioxygen is the first species involved in the oxidation. More surprisingly is, however, the influence of DMSO that also inhibits in about 85 % benzyl alcohol oxidation. This indicates that through a series of consecutive electron reduction-protonation, $O_2^{\cdot-}$ most probably evolves to the formation of H_2O_2 that would generate $\cdot$OH radicals that would be responsible for most of the observed benzyl alcohol oxidation. Scheme 2 summarizes our proposal.
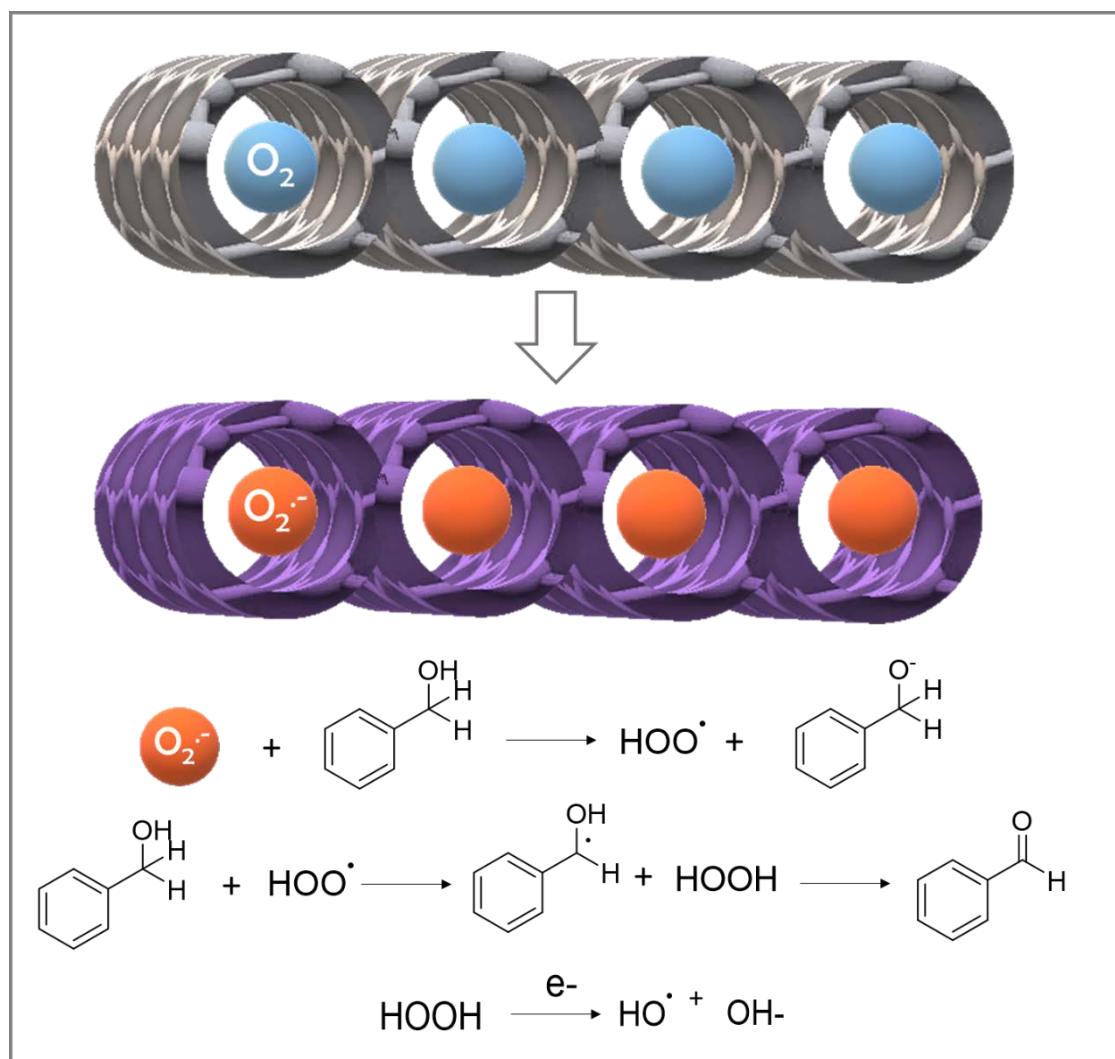
Scheme 2. Simplified reaction mechanism showing the initial generation of superoxide (in orange) within the channels from molecular O_2 (in blue) and subsequent generation of hydroxyl radicals.

Quantum Chemical Calculations

In order to understand the reasons for the different gas adsorption on $G_{\alpha\text{-CD}}$ and its higher catalytic activity to promote aerobic alcohol oxidations compared to the other congeners, theoretical DFT calculations were carried out at PBE-D3/def2-SVP level. For this purpose, three kinds of defect-free G_{CD} nanotubes ($G_{CD\text{-}1}$ to $G_{CD\text{-}3}$) were firstly built to establish the possible influence of the pore size on the adsorption of N_2 and Ar gases. Of note is that the pore dimensions and lengths of the models

do not coincide with the experimental data. The models were built to provide insights into the trend in the influence of the pore dimension at a reasonable computational cost. The energy of these systems when N_2 and Ar molecules pass through the G_{CD} tube was determined (Figure 4).

In general, contacts between N_2 or Ar and the edge of G_{CD} tubes provided a local stabilization (up to –0.2 eV) due to the interplay between these molecules and the hydrogen atoms of the surface periphery of the tubular models. Despite this fact, the results for G_{CD-1} (Figure 4A), with the smallest pore size (0.38 nm), show that the interaction of N_2 and Ar with the tubes are unfavorable. The estimated barriers for entering these gases inside the tube suggest that these energies cannot to be reached even at room temperature. Our second model G_{CD-2} presents a higher pore size (0.54 nm) than G_{CD-1}. Based on the adsorption profile (Figure 4B) and the calculated energy barrier (up to 0.85 eV for Ar), it could be possible that this pore size would allow both gases to enter inside the G_{CD-2} model at room temperature. However, neither N_2 nor Ar should not give any surface area value since isothermal adsorptions are carried out at 77 K, and therefore, the energy barrier of G_{CD-2} is too high to be reached under these conditions.
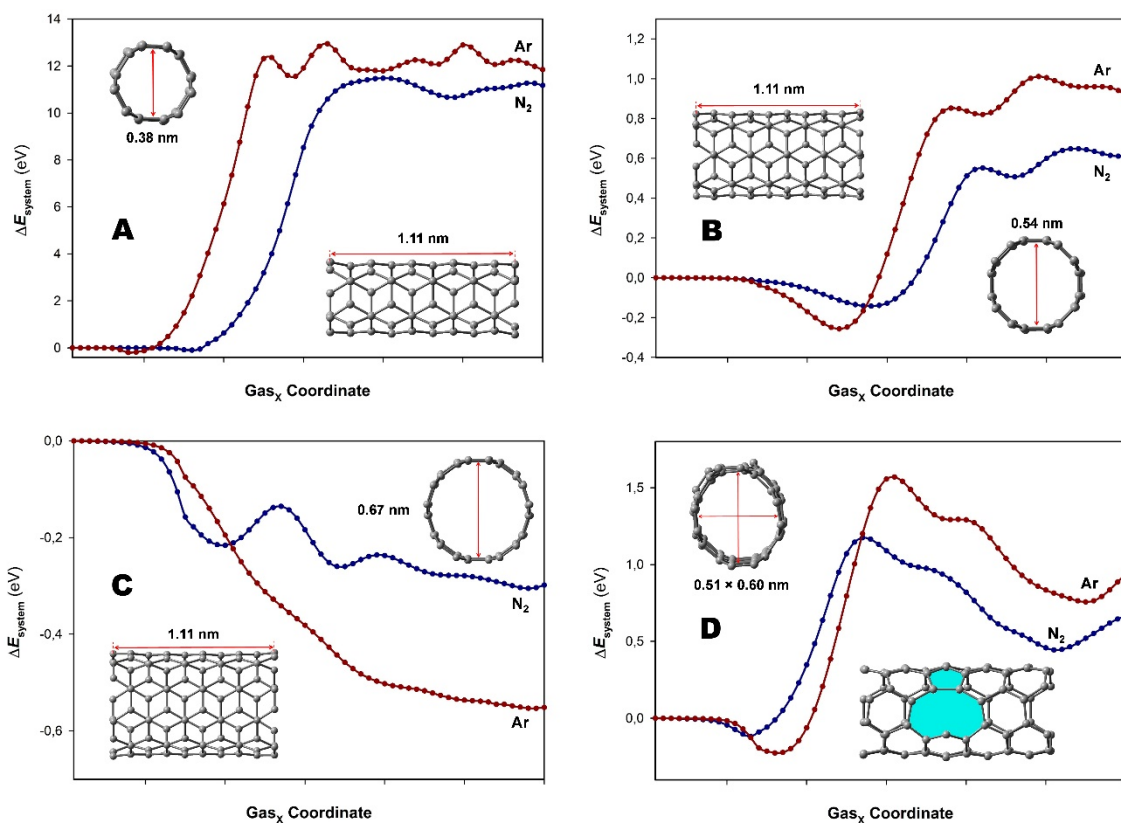
Figure 4. Theoretical adsorption profiles of N_2 and Ar gases for four different G_{CD} models: (A) G_{CD-1}; (B) G_{CD-2}; (C) G_{CD-3} and (D) defective G_{CD-2} material. Hydrogen atoms at the opening of the tubes are omitted for clarity.

The last pore size studied (0.67 nm) corresponds to G_{CD-3} model as shown in Figure 4C. The calculated profile reveals that this material perfectly allows the adsorption of both gases even at temperatures below 298 K. In addition, the interplay between G_{CD-3} tube and N_2(Ar) follows the expected trend taking into account the kinetic diameter of these gases. Thus, the lower kinetic diameter of Ar (0.340 nm) than N_2 (0.364 nm) induces that Ar fits better inside the tube being stabilized up to –0.15 eV regarding N_2.

Using our experimental findings as jumping-off point, G_{CD-2} was selected (pore size of 0.54 nm) to further understand the activation of O_2 molecule. It is known that the activation of different molecules such as H_2 or O_2 by graphene can take place at carbon atom vacancies (V_c) [37] that is a probable defect of $G_{\alpha-CD}$. As commented, Raman spectra of G_{CD} materials shows the expected peaks

corresponding to defective graphenes and the high C content of $G_{\alpha\text{-CD}}$ makes oxygenated functional groups as less probable. For that reason, a monovacancy was optimized on $G_{CD\text{-}2}$ model resulting on the appearance of a 5- and another 9-membered ring, that means, a 5/9 vacancy (Figure 4D).

As commented above, the surface area of $G_{\alpha\text{-CD}}$ could be determined using CO_2. Therefore, besides N_2 and Ar, it was of interest to compute the adsorption profiles of CO_2 gas for both defect-free and defective materials. The results obtained indicate that CO_2 can diffuse at room temperature in both defect-free and defective $G_{CD\text{-}2}$ models (Figure 5A) in agreement with experimental findings.

The introduction of one vacancy on the surface provokes different features. Firstly, a distortion of $G_{CD\text{-}2}$ tube that slightly changes the pore size (0.51 × 0.60 nm) modifying the adsorption profile and the energy barrier for entering inside the tube (Figure 4D and 5A). Secondly, MEP surfaces show a local negative region (−1.6 eV) around the vacancy hole in comparison to defect-free model (Figure 5B). The carbon vacancy defect and its surroundings have a direct influence on adsorptions of N_2, Ar and CO_2 gases stabilizing them at this position. Therefore, the presence of defects is envisioned optimal for activation of O_2 molecules inside the carbon tube. In this context, a ΔE_{ads} value of −9.6 kcal/mol points toward a favorable stabilization of O_2 on the vacancy hole (Figure 5C). In addition, other parameters also lead to an effective activation of O_2 molecule since a slight lengthening of O=O bond (ΔR = 0.02 Å) was calculated as well as a difference of density charge between oxygen atoms (Mulliken charge difference = 0.04 a.u.).
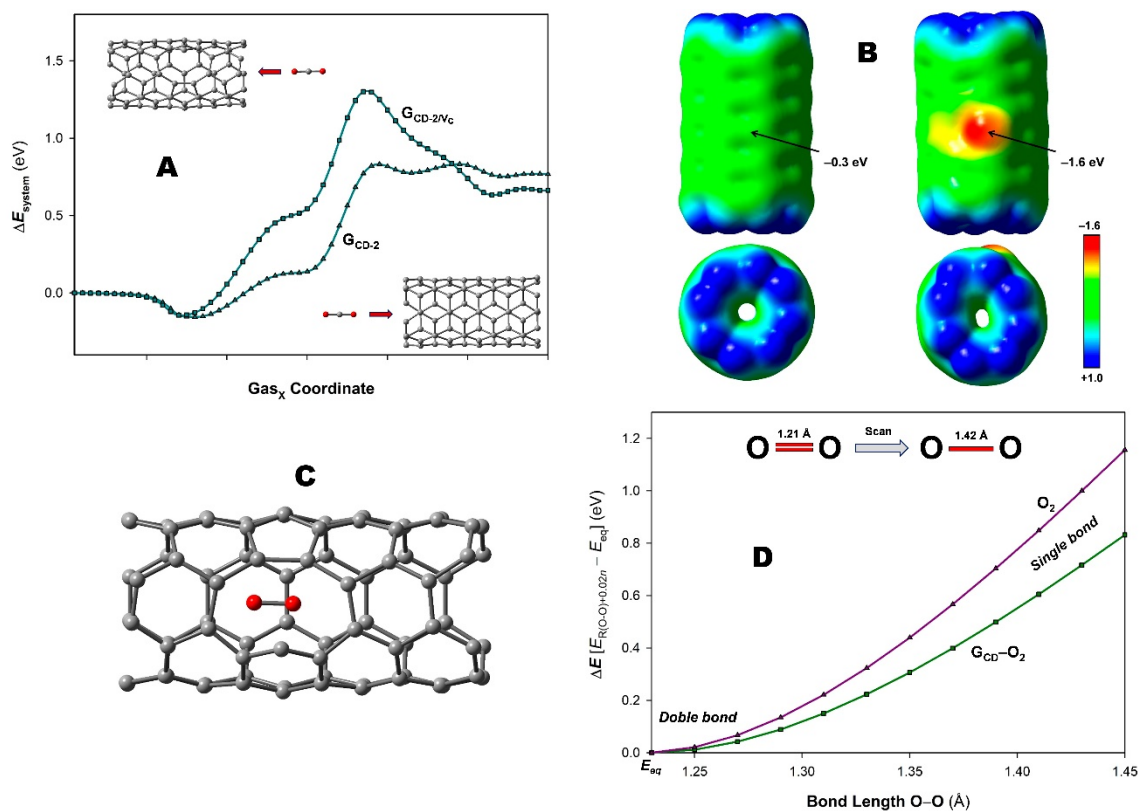
Figure 5. Theoretical outcomes at PBE-D3/def2-SVP level for: (A) adsorption profiles of CO_2 gases for G_{CD-2} and $G_{CD-2/Vc}$ materials; (B) MEP surfaces (0.001 a.u.) of G_{CD-2} (left) and $G_{CD-2/Vc}$ material (right); (C) Adsorption of a ground state O_2 molecule on a carbon monovacancy; and (D) plot of bond energy increment respect to the O=O value as a function of the O–O bond length either in *vacuum* and in the interior of G_{CD} tube.

The activation of a ground state O_2 molecule should proceed through a remarkable lengthening of O–O bond length from a double O=O bond to single O–O bond. The main feature of G_{CD} material arise from the capability to stabilize O_2 molecules, while lengthening of O–O is taking place (Figure 5D). In fact, the penalty caused by the lengthening of O–O bond inside the tube is only 0.5 eV (11.5 kcal/mol) at bond lengths around 1.40 Å whereas a penalty of 0.7 eV (16.2 kcal/mol) was found for single O_2 molecule *in vacuum*. Thus, O_2 activation is easier inside the G_{CD} tube.

Conclusions

It has been shown that pyrolysis of α, β and γ cyclodextrins forms microporous graphitic particles with regular channel dimensions that are correlated with the diameter of the cyclodextrin precursor. Particularly, in the case of $G_{\alpha\text{-CD}}$ the discrepancy between isothermal N_2 and Ar adsorption with that of CO_2 at the same temperature indicates that this material is the one in the series exhibiting ultramicroporosity able to discriminate between the kinetic dimensions of these gases. Molecular modeling shows the adsorption energy of N_2 molecules inside a cylindric tube of hexagonal sp^2 carbon atoms depends on the diameter of the tube in the range from 0.38 to 0.67 nm, there being a threshold that makes possible the entrance of N_2 inside the tube. Interaction with O_2 indicates that bond elongation resulting in the formation of superoxide is less uphill when there is a tight fit of O_2 inside the graphene channels.

In accordance with the general activity of carbonaceous materials as oxidation catalysts, all the three G_{CD} promote the aerobic oxidation of benzyl alcohol in the presence of base. However, it was observed that the initial reaction rate correlates with the pore diameter. $G_{\alpha\text{-CD}}$ is the most effective of the series and is able to promote the aerobic oxidation of benzylic primary and secondary as well as aliphatic alcohols, through a mechanism that involves the initial formation of superoxide and where ·OH radicals contribute about 85 %.

The present results illustrate the possibility to form structured graphitic carbons with regular microporosity in the subnanometric range starting from cyclodextrins. It can be predicted that the same methodology can be applied for other hollow organic capsules and their derivatives.

Experimental Section

Methods

G$_{CD}$ Preparation

Pyrolysis of commercial cyclodextrins (Aldrich) was carried out using an electric horizontal oven under N$_2$ flow (200 ml × min^{-1}) and using the following heating program: annealing at 300 ° C for 2 h by increasing the temperature from room temperature at a rate of 5 ^{o}C×min^{-1}, then heating at 1 ° C ×min^{-1} up to 900 ° C and a holding time of 2 h. Then, the sample was cooled down at room temperature maintaining the N$_2$ flow.

Catalytic measurements

10 mg of the corresponding catalyst (G$_{\alpha\text{-}CD}$, G$_{\beta\text{-}CD}$, G$_{\gamma\text{-}CD}$) dispersed in 2,5 mL of toluene were introduced into a reactor vessel (5 mL). Subsequently, the alcohol reagent (1 mmol) was added to the reactor with 1 eq of NaOH. The system was pressurized with O$_2$ (5 atm). In all cases, the reactions were carried out at 160 ^{0}C under magnetic stirring.

   Selective radical quenching experiments were carried out following the general reaction procedure described, but with the addition of radical quenchers (20 mol % with respect to the substrate). In this case, dimethylsulfoxide (DMSO) and p-benzoquinone were added as selective hydroxyl or superoxide/hydroperoxyl radical scavengers, respectively.

Product analysis

Previously filtered reaction aliquots were diluted in toluene containing a known amount of nitrobenzene as external standard. The aliquots were immediately analyzed by gas chromatography using a flame ionization detector. Quantification was carried out using calibration curves of authentic

samples against nitrobenzene as standard. Mass balances for all the reactions were higher than 95 %. Product yields can be estimated by multiplying conversion by selectivity.

Physicochemical characterization

Raman spectra were recorded with a 514 nm laser excitation on a Renishaw Raman spectrometer ("Refelx") equipped with a Leica optical microscopy and a CCD camera. The laser power in the sample was 25 mW. Each spectrum was the average of 20 acquisitions.

XPS measurements were carried out in a SPECS instrument, which includes an XPS spectrometer equipped with a monochromatic X-ray source Al Kα1 (photonic energy 1486.74 eV), operating under ultra-high vacuum at 1.3×10^{-13} atm. The photoelectrons were collected by a 150 mm radio Phoibos electron analyzer with a step energy of 30 eV. The binding energies were corrected for surface charge effects during measurements using the central level of C1s (284.5 eV) as internal reference. The elementary analyzes (EA) were carried out with a Euro EA 3000.

Thermogravimetric analysis was performed using a Mettler Toledo TGA / SDTA 851 station in the temperature range of 25-900 °C with a scanning speed of 10 ° C min^{-1} and an N$_2$ flow of 30 ml min^{-1}.

TEM images were recorded on a JEOL JEM 2100F with an acceleration voltage of 200 kV. Isothermal CO$_2$ adsorption measurements were performed using an IGA-3 gravimetric analyzer (Hiden Isochema). Adsorption measurements were carried out at 283 K. XRD pattern was recorded using a a Cubix-pro PANalytical diffractometer.

Computational details

Theoretical calculations were carried out by means of the Gaussian 16 program package. Geometry optimization were performed using the pure Perdew, Burke and Ernzerhof functional[38] selecting the Ahlrichs basis set def2-SVP.[39] In addition, density fitting approximation was automatically generated and used. Previous theoretical studies[40] regarding single-walled carbon nanotubes (SWNTs) revealed that dispersion forces dominate the adsorption of CO_2 molecules inside the tube, therefore D3 version of Grimme's empirical dispersion correction[41] was also applied. Molecular Electrostatic Potential (MEP) surfaces were also calculated at the same level of theory and plotted onto the van der Waal surface (0.001 a.u. isodensity value).

In all models, the carbon tube models have a constant length of 1.11 nm, whereas the diameter was changed from 0.38 to 0.67 nm to simulate $G_{\alpha\text{-}CD}$ material. Edges of these models are formed by hydrogen atoms, but they were omitted for clarity. For calculation of adsorption profiles, the corresponding gas (N_2, Ar or CO_2) was located outside the tube at a non-interacting distance (*ca.* 11 Å), and then, the resulting geometry was optimized to obtain a structure corresponding to a minimum (N_{imag} = 0). After that, single points calculations were performed to scan the X coordinate for N_2/Ar/CO_2 from *out* to *in* the tube modelling the structure of G_{CD}. These structures are denoted as G_{CD}-N_2(Ar or CO_2) complexes (step size from 0.5 to 0.2 Å). The energy (given in eV) of each profile point was referred to the calculated minimum structure.

Supporting information

Supporting information is available from Wiley Online Library or from the author

References

[1]   X. Cao, Y. Shi, W. Shi, G. Lu, X. Huang, Q. Yan, Q. Zhang, H. Zhang, *Small* **2011**, *7*, 3163-8.
[2]   B. G. Choi, M. H. Yang, W. H. Hong, J. W. Choi, Y. S. Huh, *ACS Nano* **2012**, *6*, 4020-8.
[3]   S. Mao, G. Lu, J. Chen, *Nanoscale* **2015**, *7*, 6924-43.
[4]   R. Munoz, C. Gomez-Aleixandre, *Chem. Vap. Deposition* **2013**, *19*, 297-322.
[5]   E. Ruiz-Hitzky, M. Darder, F. M. Fernandes, E. Zatile, F. J. Palomares, P. Aranda, *Adv. Mater. (Weinheim, Ger.)* **2011**, *23*, 5250-5.
[6]   L. Zhang, F. Zhang, X. Yang, G. Long, Y. Wu, T. Zhang, K. Leng, Y. Huang, Y. Ma, A. Yu, Y. Chen, *Sci. Rep.* **2013**, *3*, 1408, 9 pp.
[7]   A. Primo, E. Sanchez, J. M. Delgado, H. Garcia, *Carbon* **2014**, *68*, 777-83.
[8]   M.-M. Trandafir, M. Florea, F. Neatu, A. Primo, V. I. Parvulescu, H. Garcia, *ChemSusChem* **2016**, *9*, 1565-9.
[9]   A. Dhakshinamoorthy, M. Latorre-Sanchez, A. M. Asiri, A. Primo, H. Garcia, *Catal. Commun.* **2015**, *65*, 10-3.
[10]   A. Primo, P. Atienzar, E. Sanchez, J. M. Delgado, H. García, *Chemical communications* **2012**, *48*, 9254-6.
[11]   H. G. Baldovi, F. Albarracin, M. Alvaro, B. Ferrer, H. Garcia, *ChemPhysChem* **2015**, *16*, 2094-8.
[12]   I. Esteve-Adell, J. He, F. Ramiro, P. Atienzar, A. Primo, H. Garcia, *Nanoscale* **2018**, *10*, 4391-7.
[13]   M. L. Bender, M. Komiyama, *Cyclodextrin Chemistry*, Springer, **1978**.
[14]   J. Szejtli, *Chem Rev* **1998**, *98*, 1743-54.
[15]   W. Saenger, *Angew. Chem.* **1980**, *92*, 343-61.
[16]   K. A. Connors, *Chem. Rev. (Washington, D. C.)* **1997**, *97*, 1325-57.
[17]   J. E. St. Dennis, P. Venkataraman, J. He, V. T. John, S. J. Obrey, R. P. Currier, M. Lebron-Colon, F. J. Sola, M. A. Meador, *Carbon* **2010**, *49*, 718-22.
[18]   F. Trotta, M. Zanetti, G. Camino, *Polym. Degrad. Stab.* **2000**, *69*, 373-9.
[19]   M. S. Mettler, S. H. Mushrif, A. D. Paulsen, A. D. Javadekar, D. G. Vlachos, P. J. Dauenhauer, *Energy Environ. Sci.* **2012**, *5*, 5414-24.
[20]   S. Navalon, A. Dhakshinamoorthy, M. Alvaro, M. Antonietti, H. García, *Chemical Society Reviews* **2017**, *46*, 4501-29.
[21]   L. M. Malard, M. A. Pimenta, G. Dresselhaus, M. S. Dresselhaus, *Phys. Rep.* **2009**, *473*, 51-87.

[22]   A. C. Ferrari, *Solid State Commun.* **2007**, *143*, 47-57.
[23]   M. Latorre-Sanchez, A. Primo, H. Garcia, *Angew. Chem., Int. Ed.* **2013**, *52*, 11813-6.
[24]   D. W. Breck, *Zeolite Molecular Sieves: Structure, Chemistry, and Use*, Wiley-Interscience, **1974**.
[25]   H. Marsh, *Carbon* **1987**, *25*, 49-58.
[26]   J. Rouquerol, F. Rouquerol, P. Llewellyn, G. Maurin, K. S. Sing, *Adsorption by powders and porous solids: principles, methodology and applications*, Academic press, **2013**.
[27]   J. C. Groen, L. A. Peffer, J. Pérez-Ramírez, *Microporous and mesoporous materials* **2003**, *60*, 1-17.
[28]   S. Navalon, A. Dhakshinamoorthy, M. Alvaro, M. Antonietti, H. Garcia, *Chem. Soc. Rev.* **2017**, *46*, 4501-29.
[29]   A. Primo, V. Parvulescu, H. Garcia, *J. Phys. Chem. Lett.* **2017**, *8*, 264-78.
[30]   A. Santiago-Portillo, J. F. Blandez, S. Navalon, M. Alvaro, H. Garcia, *Catal. Sci. Technol.* **2017**, *7*, 1351-62.
[31]   A. Santiago-Portillo, M. Cabrero-Antonino, M. Alvaro, S. Navalon, H. Garcia, *Chem. - Eur. J.* **2019**, *25*, 9280-6.
[32]   M. T. Maurette, E. Oliveros, P. P. Infelta, K. Ramsteiner, A. M. Braun, *Helv. Chim. Acta* **1983**, *66*, 722-33.
[33]   H. J. Guiraud, C. S. Foote, *J. Am. Chem. Soc.* **1976**, *98*, 1984-6.
[34]   L. Li, Y. Abe, K. Kanagawa, N. Usui, K. Imai, T. Mashino, M. Mochizuki, N. Miyata, *Anal. Chim. Acta* **2004**, *512*, 121-4.
[35]   S. E. Page, W. A. Arnold, K. McNeill, *J. Environ. Monit.* **2010**, *12*, 1658-65.
[36]   J. C. Espinosa, S. Navalon, M. Alvaro, H. Garcia, *ChemCatChem* **2016**, *8*, 2642-8.
[37]   A. Primo, A. Franconetti, M. Magureanu, N. B. Mandache, C. Bucur, C. Rizescu, B. Cojocaru, V. I. Parvulescu, H. Garcia, *Green Chem.* **2018**, *20*, 2611-23.
[38]   J. P. Perdew, K. Burke, M. Ernzerhof, *Phys. Rev. Lett.* **1996**, *77*, 3865-8.
[39]   F. Weigend, R. Ahlrichs, *Phys. Chem. Chem. Phys.* **2005**, *7*, 3297-305.
[40]   D. Quinonero, A. Frontera, P. M. Deya, *J. Phys. Chem. C* **2012**, *116*, 21083-92.
[41]   S. Grimme, J. Antony, S. Ehrlich, H. Krieg, *J. Chem. Phys.* **2010**, *132*, 154104/1-/19.